

xQSM – Quantitative Susceptibility Mapping with Octave Convolutional Neural Networks

Yang Gao, Xuanyu Zhu, Stuart Crozier, Feng Liu, Hongfu Sun

Abstract—Quantitative susceptibility mapping (QSM) is a valuable magnetic resonance imaging (MRI) contrast mechanism that has demonstrated broad clinical applications. However, the image reconstruction of QSM is challenging due to its ill-posed dipole inversion process. In this study, a new deep learning method for QSM reconstruction, namely xQSM, was designed by introducing modified state-of-the-art octave convolutional layers into the U-net backbone. The xQSM method was compared with recently-proposed U-net-based and conventional regularization-based methods, using peak signal to noise ratio (PSNR), structural similarity (SSIM), and region-of-interest measurements. The results from a numerical phantom, a simulated human brain, four *in vivo* healthy human subjects, a multiple sclerosis patient, a glioblastoma patient, as well as a healthy mouse brain showed that the xQSM led to suppressed artifacts than the conventional methods, and enhanced susceptibility contrast, particularly in the iron-rich deep grey matter region, than the original U-net, consistently. The xQSM method also substantially shortened the reconstruction time from minutes using conventional iterative methods to only a few seconds.

Index Terms—quantitative susceptibility mapping, xQSM, dipole inversion, deep learning, octave convolution

I. INTRODUCTION

QUANTITATIVE susceptibility mapping (QSM) is an MRI post-processing technique, which extracts tissue magnetic susceptibility from MRI phase images [1], [2]. It has shown great potential for studying a variety of neurological disorders, such as Multiple Sclerosis [3], [4], [5], Alzheimers disease [6], Parkinson’s disease [7], alcohol use disorders [8], and intracranial hemorrhage [9], [10]. However, QSM reconstruction is non-trivial, which involves several key post-processing steps [1], [2]. For example, the gradient-echo raw phase images from multiple receivers need to be correctly combined [11] and unwrapped [12]. Background magnetic field contribution from outside of the brain should be removed [13], [14], [15], [16]. Dipole inversion is then performed, which is an ill-posed inverse problem.

Different methods have been proposed to solve the ill-posed dipole inversion. One method uses multiple orientation sampling to compensate for the missing data in a single orientation, which is known as the Calculation of Susceptibility through Multiple Orientation Sampling (COSMOS) [17]. This method requires at least three different head orientations to solve the dipole deconvolution analytically. Although

this method is considered as the gold standard except for anisotropic white matter [18], the time-consuming repeated scans and the requirements for patients to rotate heads hinder its feasibility. Therefore, iterative methods such as iLSQR [19], morphology enabled dipole inversion (MEDI) [20], and total field inversion methods [21], [22], [23] were developed to restore high-quality susceptibility maps from single orientation measurements. However, these methods can be computationally intensive, time-consuming, and require manual parameter tuning for different datasets.

Recently, deep learning has been applied to solve a variety of inverse problems [24] as an alternative to the conventional iterative methods, owing to its capability to approximate any continuous function, given enough learnable parameters and large datasets [24], [25]. It has also been reported that deep neural networks can achieve superior performance than the state-of-the-art iterative methods in super-resolution [26], denoising [27], deconvolution [28], and image reconstruction tasks [29], [30]. The hypothesis [31], [32], [24] is that compared with traditional methods using explicitly designed regularization, deep neural networks can learn more effective data-driven regularization to preserve anatomical structures more accurately. Lastly, deep learning-based image reconstructions are generally fast [24], [31], which is a critical advantage in practice.

Previous studies [33], [34], [35], [36] have successfully trained multiple deep neural networks for QSM dipole inversion. QSMnet [33] trained a 3D U-net [37] with single-orientation local field and COSMOS maps as inputs and labels. QSMGAN [34] further improved this scheme by adding a discriminator on the U-net to construct a Generative Adversarial Network (GAN) [38]. However, these methods did not consider the susceptibility anisotropy effects when using COSMOS as the training labels. AutoQSM [35] proposed to train a U-net that could restore brain tissue QSM directly from the total field maps without explicit skull stripping and background field removal. The training inputs were single-orientation local field maps, while the training labels were QSM images reconstructed using the two-step STAR-QSM [39] method, which preserved the susceptibility anisotropy. All the above three frameworks require reconstructing QSM first using conventional iterative methods as the training labels; however, these assigned labels may not be the ground truth due to reconstruction errors. In contrast, another deep learning framework, DeepQSM [36], generated local field maps from synthetic QSM labels of simple geometric shapes using the forward model [13], [40] so that the training inputs and labels satisfy the exact underpinning equation between susceptibility

Yang Gao, Xuanyu Zhu, Stuart Crozier, Feng Liu and Hongfu Sun are with the School of Information Technology and Electrical Engineering, the University of Queensland, Brisbane, Australia

Correspondence: Hongfu Sun, Address: Room 538, General Purpose South (Building 78), University of Queensland, St Lucia QLD 4072; Email: hongfu.sun@uq.edu.au

source and induced field. However, susceptibility underestimation was reported in DeepQSM [36], especially in deep grey matter (DGM) regions.

Octave Convolution (OctConv) [41] is a recently proposed operation, aiming to reduce the substantial redundancy that exists in the spatial dimension of feature maps generated in deep convolutional neural networks (CNNs). OctConv explicitly factorizes the feature maps in CNNs into high and low spatial resolution groups, which corresponds to the fact that natural images can be decomposed into high- and low-frequency components. It has been reported [41] that this design can improve the efficiency of the networks and accomplish better multi-scale representation for various image and video tasks. In this study, we propose an enhanced U-net framework, namely xQSM, for reconstructing QSM via replacing the traditional convolutional layers with modified OctConv layers, to recover the susceptibility contrast loss in the original U-net based method. Similar to the DeepQSM [36] method, local field maps generated using the forward model calculation from training labels are used as training inputs. We also investigate the effects of training with *in vivo* brain QSM data containing sophisticated brain structures, as compared to training with synthetic QSM data containing only simple shapes.

II. METHODS

A. Ill-posed QSM Dipole Inversion

The tissue with magnetic susceptibility distribution $\chi(\mathbf{r})$, where \mathbf{r} denotes the spatial location, when placed in the main field B_0 (applied along the z-direction) of an MRI scanner, will gain a magnetization in the z-direction $M_z(\mathbf{r}) \approx \chi(\mathbf{r}) \cdot B_0 / \mu_0$, where μ_0 is the vacuum permeability. This tissue magnetization will generate a perturbation field $\Delta\mathbf{B}(\mathbf{r})$, which can be formulated as:

$$\Delta\mathbf{B}(\mathbf{r}) = \frac{\mu_0}{4\pi} \int d^3\mathbf{r}' \left\{ \frac{3(\mathbf{r}-\mathbf{r}') \cdot \mathbf{M}(\mathbf{r}') \cdot (\mathbf{r}-\mathbf{r}')}{|\mathbf{r}-\mathbf{r}'|^5} - \frac{\mathbf{M}(\mathbf{r}')}{|\mathbf{r}-\mathbf{r}'|^3} \right\} \quad (1)$$

when only considering the calculation in z-direction, (1) can be simplified as:

$$\Delta B(\mathbf{r}) = \chi(\mathbf{r}) \otimes d(\mathbf{r}) \cdot B_0 \quad (2)$$

where $d(\mathbf{r}) = (3\cos^2\theta - 1)/(4\pi|\mathbf{r}|^3)$ is referred to as the dipole kernel, and θ is the angle between $\mathbf{r} - \mathbf{r}'$ and the main field B_0 (z-direction); \otimes represents the convolution operation. This equation suggests that the induced magnetic field perturbation equals to the convolution of the magnetic susceptibility source with the unit dipole kernel. Such a relationship can be simplified as multiplication in the k-space [13], [23], [40]:

$$D(\mathbf{k}) \cdot \chi(\mathbf{k}) = \frac{\Delta B(\mathbf{k})}{B_0} \quad (3)$$

where $D(\mathbf{k}) = 1/3 - k_z^2/(k_x^2 + k_y^2 + k_z^2)$ ($D = 0$ at the origin) is the unit dipole kernel in k-space, and $\mathbf{k} = (k_x, k_y, k_z)$ are the k-space coordinates.

Equation (3) depicts the key concept of QSM dipole inversion, which is an ill-posed inverse problem because of the zero values of dipole kernel $D(\mathbf{k})$ on a double conical surface

($k_x^2 + k_y^2 = 2k_z^2$). On the other hand, it also served as a well-posed forward model for preparing the training datasets in this work.

B. Octave Convolution

In this study, we modified the original OctConv [41] by replacing the nearest-neighbor interpolation with a transposed convolution to allow for more learnable parameters. As illustrated in the middle row of Fig. 1, the new OctConv is formulated as a combination of 8 basic operations (i.e., four 3D traditional convolutions, one 3D average pooling, one 3D transposed convolution, and two additions):

$$\begin{aligned} Y_H &= F_{HH} + F_{LH} \\ Y_L &= F_{HL} + F_{LL} \\ F_{HH} &= \text{Conv}_{HH}(X_H) \\ F_{HL} &= \text{Conv}_{HL}(\text{AvgPool}(X_H)) \\ F_{LH} &= \text{ConvT}(\text{Conv}_{LH}(X_L)) \\ F_{LL} &= \text{Conv}_{LL}(X_L) \end{aligned} \quad (4)$$

where $\text{Conv}()$ represents convolution operations with subscripts indicating different kernels (i.e., H for High resolution and L for Low resolution); $\text{ConvT}()$ represents the conventional transposed convolution of kernel size 2, which doubles the resolution of feature maps; $\text{AvgPool}()$ is the average pooling operation of stride 2, which halves the resolution of feature maps; $X \in \mathbb{R}^{\tilde{h} \times \tilde{w} \times \tilde{d} \times c}$ denotes the input feature maps in traditional convolution networks, where \tilde{h} , \tilde{w} , \tilde{d} , and c represent the height, width, depth, and channels of this feature, respectively. The OctConv explicitly factorizes the feature maps into two spatial resolution groups $\{X_H, X_L\}$ along the channel dimension, where $X_H \in \mathbb{R}^{\tilde{h} \times \tilde{w} \times \tilde{d} \times \alpha_x c}$ represents high spatial resolution group and $X_L \in \mathbb{R}^{\frac{\tilde{h}}{2} \times \frac{\tilde{w}}{2} \times \frac{\tilde{d}}{2} \times (1-\alpha_x)c}$ is the low spatial resolution group, and α_x is a ratio factor. Similarly, the output features $Y \in \mathbb{R}^{\tilde{h} \times \tilde{w} \times \tilde{d} \times c}$ in traditional convolutions can also be decomposed into $\{Y_H, Y_L\}$ and serve as inputs to the next OctConv layer. In this work, the ratio factor α_x and α_y was set to 0.5 for input and output feature maps of all the middle layers. For the first layer, α_x (input) was set to 1 and α_y (output) was set to 0.5 to convert the conventional feature maps into octave feature maps. For the last OctConv layer, α_x was set to 0.5 and α_y was set to 1, resulting in a single high-resolution output [41].

C. xQSM Deep Neural Network

The proposed xQSM network is an enhanced 3D U-net with all conventional convolutions replaced with the new OctConv, as shown in Fig. 1. The xQSM network contains 10 OctConv layers (3^3 kernel size with stride 1), 2 max-pooling layers (2^3 kernel size with stride 1), 2 transposed convolution layers (2^3 kernel size with stride 2), 12 batch normalization layers, and 1 final convolution layer (1^3 kernel size with stride 1). The rectified linear unit (ReLU) [42] is adopted as the activation function of the network.

Similar to the original U-net, the xQSM network comprises two CNNs, a contracting part and an expanding part, also referred to as the down-sampling (encoder) path and the

xQSM Framework (*in vivo* dataset)

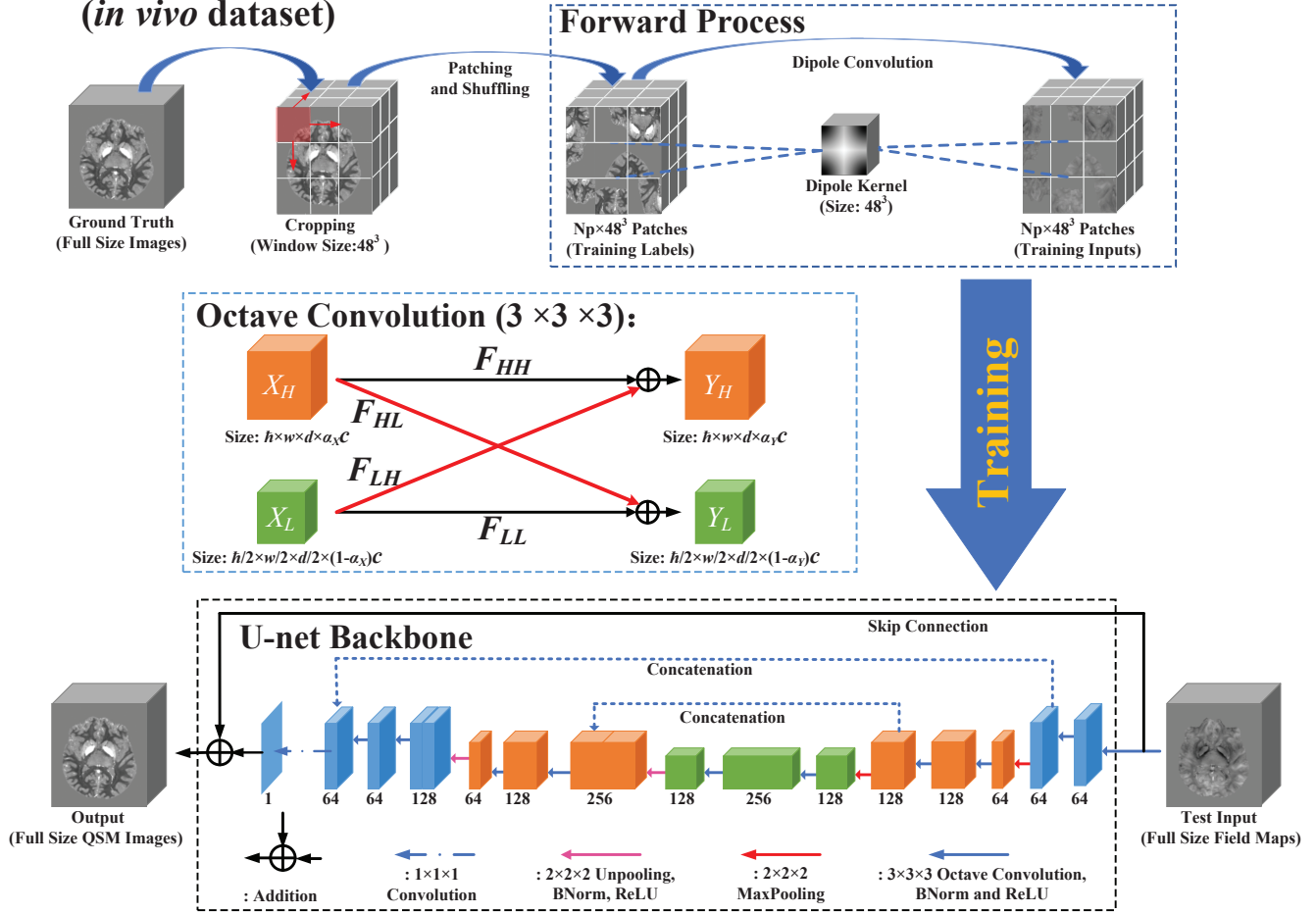


Fig. 1. The top row demonstrates the preparation process of the *in vivo* training datasets. Octave convolution is shown in the middle row, which introduces an X-shaped operation for communication between feature maps of different resolutions. The bottom row illustrates the xQSM network architecture based on the U-net backbone.

up-sampling (decoder) path, respectively. The resolutions of feature maps in the middle layers are smaller than that of the former and latter layers. Such a design can improve the efficiency of the network and reduce the memory cost during training. This advantage is further enhanced with our modified OctConv as implemented in xQSM, since feature factorization reduces the redundancy of deep networks as described above. The proposed xQSM also has two concatenations from layers of contracting parts to expanding parts as introduced in the backbone U-net, which compensate for the spatial information loss after max-pooling layers. The concatenation design can mitigate the gradient vanishing problem and improve network performance [32].

The proposed xQSM also adds a skip connection between the input and the output, forming a residual block [43], which helps the training process converge faster. The skip connection can also mitigate the vanishing gradient problem during training [44] and provide a noticeable performance enhancement compared to networks without residual connections [32].

D. Data Preparation

Local field maps, as training inputs, were generated via convolving the QSM labels with the unit dipole kernel according to the forward model (3), which is consistent with the DeepQSM study [36]. Two sets of QSM labels were tested: one set from *in vivo* QSM brain volumes acquired from 90 healthy subjects (1 mm isotropic resolution) and reconstructed with the iLSQR method [19], and another set from synthetic digital phantoms containing basic geometric shapes (spheres, squares, and rectangles) as described in the DeepQSM paper [36].

QSM datasets were cropped into small patches to fit into GPU memory for training. For *in vivo* dataset preparation, as shown in the top row of Fig. 1, the full-size ($144 \times 196 \times 128$) *in vivo* QSM volumes were cropped into small patches (size 48^3) via firstly sliding a 48^3 cropping window with a stride of $24 \times 36 \times 20$ to traverse the 90 iLSQR-QSM and obtain 11250 patches, and then randomly cropping 3750 more patches from all 90 subjects (around 41-42 from each subject). After the cropping, the corresponding local field maps of the same size, i.e., 48^3 , were calculated according to the forward model (3).

In total, 15,000 *in vivo* susceptibility patches (size 48^3) and their corresponding field maps were generated, as labels and inputs. For the synthetic dataset, we directly simulated 15,000 volumes of synthetic phantoms (size 48^3) as described in the DeepQSM paper [36], and then calculated their corresponding field maps. Both xQSM and the original U-net (i.e., the network used in DeepQSM [36]) were trained on the two sets of QSM data (i.e., *in vivo* and synthetic). We refer to these networks as xQSM_{in vivo}, U-net_{in vivo}, xQSM_{synthetic}, and U-net_{synthetic} based on different network structures and training dataset types.

E. Network Training

The xQSM network is optimized via minimizing the following L2-norm loss function:

$$\arg \min_{\theta} \frac{1}{2N} \sum_{i=1}^N \|C(X_i; \theta) - Y_i\|_F^2 \quad (5)$$

where $\{X_i, Y_i\}_{i=1}^N$ denotes the N number training inputs and labels; $\|\cdot\|_F^2$ is the Frobenius norm; θ represents the hyper-parameters of the networks; $C(X_i; \theta)$ is the output of the current deep neural network. In this study, each network was trained for 14-18 hours (i.e., 100 epochs) using 2 Tesla V100 GPUs with a mini-batch size of 32. All weights and biases were initialized with normally distributed random numbers with a mean of zero and a standard deviation of 0.01.

The network parameters were optimized using Adaptive moment estimation (Adam) [45]:

$$\begin{aligned} \theta_t &= \theta_{t-1} - \eta \frac{\hat{m}_t}{\sqrt{\hat{v}_t} + \epsilon} \\ \hat{m}_t &= \frac{m_t}{1 - (\beta_1)^t} \\ \hat{v}_t &= \frac{v_t}{1 - (\beta_2)^t} \\ m_t &= \beta_1 m_{t-1} + (1 - \beta_1) g_t \\ v_t &= \beta_2 v_{t-1} + (1 - \beta_2) g_t^2 \end{aligned} \quad (6)$$

where t represents current mini-batch; g_t is the gradient for the parameters on current mini-batch; m_t and v_t are the biased estimates for the first moment and second raw moment on current iteration, which are initialized with zeros; \hat{m}_t and \hat{v}_t are the bias-corrected estimates for the first moment and

second raw moment on current step; η is the learning rate and was set to 10^{-3} , 10^{-4} , and 10^{-5} for the first 50 epochs, 50-80 epochs, and final 20 epochs respectively; β_1 , β_2 , and ϵ are hyper-parameters and were set to their default values (i.e., $\beta_1 = 0.9$, $\beta_2 = 0.999$, and $\epsilon = 10^{-8}$).

The proposed xQSM network were implemented using MATLAB R2019a and Pytorch 1.1 independently. The source codes are published at <https://github.com/sunhongfu/deepMRI/tree/master/xQSM>.

F. Validation with Simulated and In vivo Datasets

Although the network is trained with cropped patches of size 48^3 , the reconstruction implementation using xQSM network is operated on full-size local field maps without cropping. Note that the size of local field maps is required to be evenly dividable by 8, and zero-padding can be performed to satisfy this requirement.

The proposed xQSM was compared with the original U-net and two conventional dipole inversion methods (i.e., iLSQR [19] and MEDI [20]) on both simulated and *in vivo* datasets.

Simulated magnetic field maps were generated by the forward model of (3), from (i) a modified 3D Shepp-Logan phantom (susceptibilities of -0.1, -0.25, -0.2, -0.05, 0.15, and 0.35 parts-per-million (ppm) for various ellipsoids as shown in Fig. 2), and (ii) a COSMOS map (age: 24 years, male) from a healthy subject reconstructed from five head orientations (1 mm isotropic at 3T). Four local field maps of two different contrast levels and two noise levels (denoted by Sim1Snr1, Sim1Snr2, Sim2Snr1, and Sim2Snr2 with ‘‘Sim’’ representing contrast levels and ‘‘Snr’’ standing for noise levels) from the 2019 QSM Challenge 2.0 (http://qsm.snu.ac.kr/?page_id=30) were also tested. Peak signal to noise ratio (PSNR), Structural similarity (SSIM) and region of interest (ROI) values were measured for the quantitative assessments of different QSM dipole inversion methods on these simulated maps.

Four *in vivo* (age: 42.4 ± 5.8 years, male) local field maps acquired from a multi-echo gradient-echo sequence were processed by the standard QSM pipeline, including phase unwrapping using the best path method [12] and background field removal using the RESHARP method [14]. Among the four *in vivo* experiments, three healthy subjects were acquired at 3T with 1 mm isotropic resolution, and another healthy subject was acquired at 7T with 0.6 mm isotropic resolution.

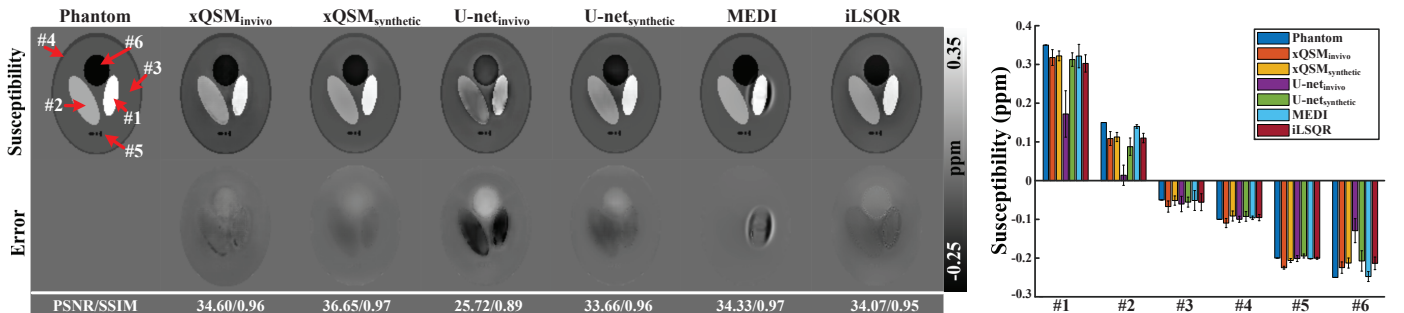


Fig. 2. Comparison of different methods on the 3D Shepp-Logan phantom. QSM results and error maps are presented along with PSNR and SSIM. The bar graph reports the corresponding ROI measurements of the six regions pointed by the red arrows.

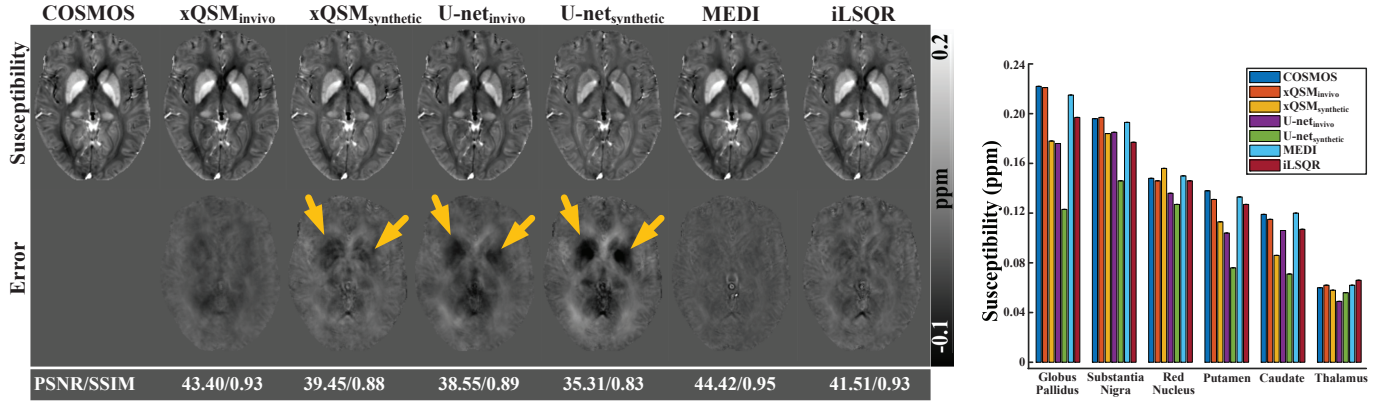


Fig. 3. Comparison of different QSM methods on a COSMOS (1 mm isotropic) simulated data. QSM results and error maps of an axial central slice are reported with the corresponding PSNR and SSIM. The corresponding ROI measurements of six deep grey matter regions are plotted in the bar graph. Yellow arrows point to significant underestimation in the corresponding reconstructions.

Different dipole inversion methods were compared. Deep grey matter susceptibilities of globus pallidus (GP), putamen (PU), caudate nucleus (CN), thalamus (TH), substantia nigra (SN), and red nucleus (RN) were measured.

Another three *in vivo* local field maps, including a multiple sclerosis (MS) patient with multiple “T1 blackhole lesions” (1 mm isotropic at 3T), a glioblastoma patient with multiple hemorrhages (0.6 mm×0.6 mm×2 mm at 3T), and a healthy mouse brain (0.1 mm isotropic at 9.4 T), processed from the standard QSM pipeline, were also tested for evaluating the generalization of the proposed xQSM network.

III. RESULTS

A. Digital Phantom Simulations

Fig. 2 compares xQSM, U-net, MEDI, and iLSQR results on a digital 3D Shepp-Logan phantom. The susceptibility and error maps from different methods showed that the U-net_{in vivo} introduced the most significant contrast loss, while

the xQSM_{synthetic} produced the best susceptibility contrast among all deep learning methods. The proposed xQSM framework also achieved the highest PSNR and SSIM (36.65/0.97 for xQSM_{synthetic} and 34.60/0.96 for xQSM_{in vivo}) among all methods. These error metrics (i.e., PSNR and SSIM) suggested that the networks trained on synthetic data performed better than *in vivo* brain datasets on these simple shapes. For example, the U-net_{synthetic} outweighed the U-net_{in vivo} with 7.94 dB and 7% improvements on PSNR and SSIM, respectively. Besides, the proposed xQSM_{in vivo} surpassed the U-net_{in vivo} with an improvement of 8.88 dB on PSNR and 7% on SSIM, which suggested that xQSM incorporating OctConv generalized better than conventional convolutions. Susceptibility measurements of all the uniform structures are displayed in the bar graph of Fig. 2, which demonstrated that the proposed xQSM_{synthetic} (in region #1 and #3) and MEDI (in the region #2, #4, #5, and #6) were the most accurate methods. The reconstruction time for this Shepp-Logan phantom (size 128³) of xQSM (synthetic and *in vivo*), U-nets (synthetic and *in vivo*), MEDI, and iLSQR were 0.61, 0.36, 107, and 21 seconds, respectively. Deep learning methods were computed on an Nvidia Tesla V100 GPU. MEDI and iLSQR were performed on a computer with 4×Intel(R) Core (TM) i7-7700HQ@2.8GHz CPU.

B. Digital Brain Simulations

Reconstruction results of xQSM, U-net, iLSQR, and MEDI for local field maps simulated from a COSMOS map (1 mm isotropic at 3T) were shown in Fig. 3. The proposed xQSM_{in vivo} showed similar PSNR and SSIM (43.40/0.93) to conventional iLSQR (41.53/0.93) and MEDI methods (44.42/0.95), while the xQSM_{synthetic}, U-net_{in vivo}, and U-net_{synthetic} substantially underestimated susceptibilities of deep grey matter (yellow arrows), especially GP with 20%, 21%, and 40% underestimation, respectively. The iLSQR method also led to around 12% underestimation in GP. The proposed xQSM_{in vivo} and MEDI methods were the only two methods without introducing noticeable contrast loss (1% and 3% underestimation of GP, respectively) in deep grey matter. Comparisons of deep learning-based methods suggested that

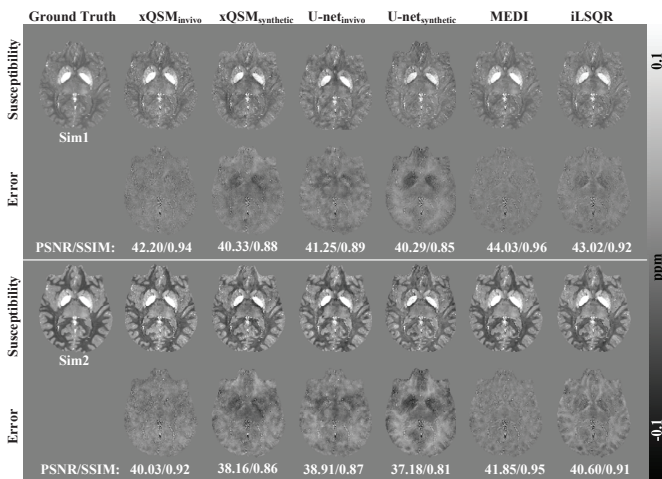


Fig. 4. Comparison of different QSM methods on the 2019 QSM Challenge data. The top two rows illustrate the reconstruction and error maps of the higher contrast level data (the average of “Sim2Snr1” and “Sim2Snr2”), while the bottom two rows demonstrate the corresponding results on low-contrast data (the average of “Sim1Snr1” and “Sim1Snr2”).

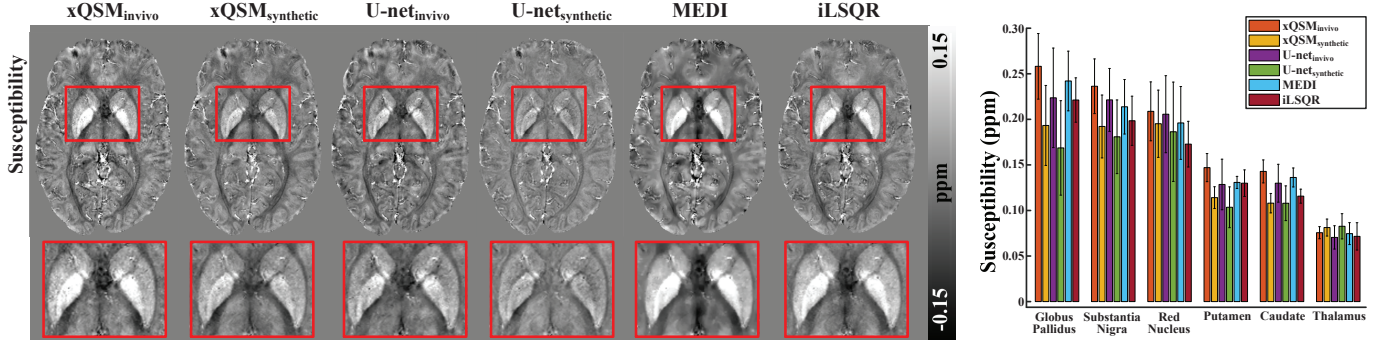


Fig. 5. Comparison of different QSM methods on an *in vivo* local field map (0.6 mm isotropic) from a healthy volunteer. The QSM results and a zoomed-in vision of deep grey matter regions are shown in the left part. The bar chart shows the ROI measurements of the six deep grey matter structures over 4 healthy subjects (including 3 more 1 mm isotropic data).

the performance of the $U\text{-net}_{\text{synthetic}}$ as proposed in the DeepQSM paper [36] can be improved via incorporating the OctConv operation as in $x\text{QSM}_{\text{synthetic}}$, using *in vivo* dataset for training as in $U\text{-net}_{\text{in vivo}}$, or implementing both OctConv and *in vivo* training dataset as in $x\text{QSM}_{\text{in vivo}}$. These three strategies resulted in 20%, 19%, and 39% of improvements in GP value. For this COSMOS test (size $192 \times 256 \times 176$), the reconstruction time of deep learning methods (about 2.4 and 1.4 seconds for xQSM and U-net) was substantially shorter than traditional methods (about 48 and 614 seconds for iLSQR and MEDI).

C. 2019 QSM Challenge Datasets

Fig. 4 compared the results of different deep learning and conventional QSM methods on the 2019 QSM Challenge 2.0 data (1 mm isotropic). The proposed $x\text{QSM}_{\text{in vivo}}$ led to the best PSNR and SSIM among the deep learning methods and comparable reconstructions to iLSQR and MEDI, in both low- (Sim1) and high-contrast (Sim2) datasets. As shown in the error maps, $x\text{QSM}_{\text{synthetic}}$, $U\text{-net}_{\text{in vivo}}$, $U\text{-net}_{\text{synthetic}}$, and iLSQR methods displayed susceptibility underestimation in deep grey matter regions, especially in GP (17%, 8%, 23%, and 12% underestimation, respectively), while $x\text{QSM}_{\text{in vivo}}$ and MEDI did not show noticeable underestimation in the region (less than 1%). Table I summarized the average ROI measurements (mean \pm standard deviation) for 2019 QSM

Challenge 2.0 data over six deep grey matter regions (GP, SN, RN, PU, CN, and TH). It was confirmed that the susceptibility underestimation in deep grey matter regions introduced by $U\text{-net}_{\text{synthetic}}$ was alleviated by incorporating the proposed OctConv (e.g., 5% improvement from $U\text{-net}_{\text{synthetic}}$ to $x\text{QSM}_{\text{synthetic}}$ and 8% improvement from $U\text{-net}_{\text{in vivo}}$ to $x\text{QSM}_{\text{in vivo}}$ for GP), or by using *in vivo* datasets (17% improvement from $x\text{QSM}_{\text{synthetic}}$ to $x\text{QSM}_{\text{in vivo}}$ and 15% improvement from $U\text{-net}_{\text{synthetic}}$ to $U\text{-net}_{\text{in vivo}}$ for GP) or implementing both strategies (23% improvement from $U\text{-net}_{\text{synthetic}}$ to $x\text{QSM}_{\text{in vivo}}$). The reconstructions of deep learning methods (about 2.2 seconds for xQSM and 1.4 seconds for U-net) were considerably faster than iLSQR and MEDI (54 and 720 seconds) for all challenge data (image size $164 \times 205 \times 105$).

D. In vivo Experiments

QSM results from an *in vivo* local field map (0.6 mm isotropic) acquired at 7T were shown in Fig. 5. The zoomed-in deep grey matter regions showed that the proposed $x\text{QSM}_{\text{in vivo}}$ led to the best reconstruction results among all deep learning methods, with the other three deep learning frameworks substantially underestimating the deep grey matter susceptibility

TABLE I
DEEP GREY MATTER ROI MEASUREMENTS OF THE 2019 QSM CHALLENGE DATA.

	GP	SN	RN	PU	CN	TH
	mean(standard deviation) in parts-per-billion					
Ground Truth	108(12)	91(1)	76(11)	31(5)	32(8)	13(5)
$x\text{QSM}_{\text{in vivo}}$	108(11)	82(6)	76(10)	27(4)	39(9)	13(4)
$x\text{QSM}_{\text{synthetic}}$	89(12)	74(1)	69(10)	17(4)	26(10)	5(2)
$U\text{-net}_{\text{in vivo}}$	99(14)	77(6)	71(16)	17(4)	30(10)	9(5)
$U\text{-net}_{\text{synthetic}}$	83(11)	79(4)	73(13)	17(3)	28(8)	9(2)
MEDI	108(14)	88(1)	79(12)	32(6)	35(9)	13(4)
iLSQR	95(13)	73(1)	71(12)	24(5)	30(9)	11(4)

The best measurements are highlighted in bold.

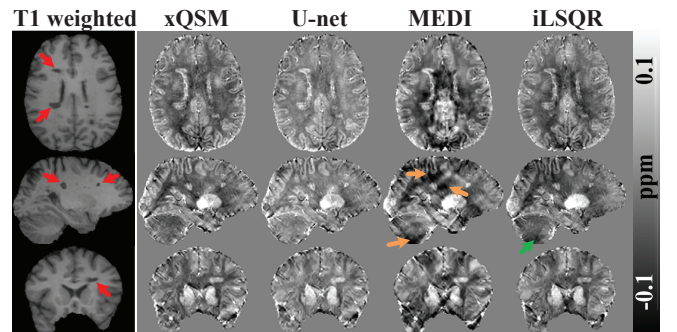


Fig. 6. Different QSM methods on an *in vivo* field map (1 mm isotropic) from a patient with multiple sclerosis. The left column shows T1 weighted magnitude images of the same patient in three orthogonal views. Red arrows point to brain lesions that are detected by different QSM methods. The orange arrows and green arrow point to the artifacts in MEDI and iLSQR methods, respectively.

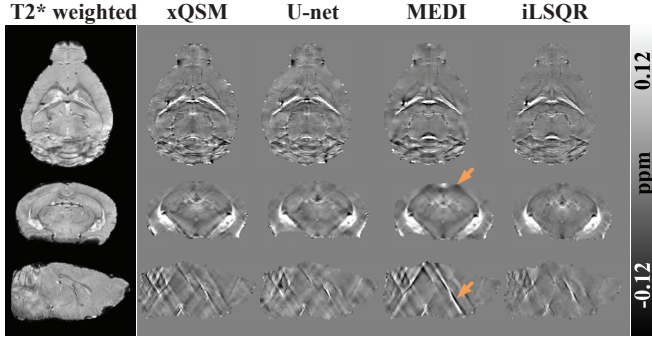


Fig. 7. Demonstration of xQSM, U-net, and traditional methods on an *in vivo* local field map from a mouse brain of ultra high resolution (0.1 mm isotropic) in three orthogonal views. The left panel illustrates the corresponding T2* weighted images. Orange arrows point to the artifacts in MEDI reconstruction.

compared to conventional methods. The QSM result from MEDI appeared blurrier due to image regularization, which may obscure small structures. For this local field map of size $224 \times 304 \times 224$, the reconstruction time of the proposed xQSM (around 4.2 seconds) and U-net (about 2.6 seconds) was much shorter than iLSQR (about 129 seconds) and MEDI (over 1000 seconds). Susceptibility measurements of six deep grey matter regions from 4 healthy subjects (including 3 more 1 mm isotropic local field maps acquired at 3T) were reported in the bar graph of Fig. 5. The proposed xQSM_{in vivo} resulted in the highest average GP susceptibility measurement, and was 25%, 15%, 35%, 15%, and 6% higher than xQSM_{synthetic}, U-net_{in vivo}, U-net_{synthetic}, iLSQR, and MEDI, respectively.

Fig. 6 demonstrated the QSM results of a MS patient using different methods in orthogonal views. The T1-weighted images were shown in the first column with red arrows pointing to multiple MS lesions, appearing as black holes. All four QSM methods successfully detected the lesions. The proposed xQSM method recovered the susceptibility contrast loss in the U-net results. Severe artifacts (orange arrow) appeared in the MEDI results, which were absent in the deep learning and iLSQR methods.

QSM results, using xQSM, U-net, MEDI, and iLSQR, of a mouse brain with a much finer spatial resolution (100 microns isotropic), were compared in Fig. 7. The xQSM and U-net appeared similar to the iLSQR method, while MEDI appeared blurry and artifactual, especially in the sagittal and coronal views (orange arrows). This figure demonstrated the generalization ability of the proposed xQSM from the human brain to the mouse brain. Although the networks were trained with 1 mm isotropic *in vivo* human brain dataset, it could be directly used to reconstruct mouse brain QSM of ultra-high resolution and different brain anatomy.

Fig. 8 illustrated different QSM reconstructions of a patient with glioblastoma (resolution of $0.6 \text{ mm} \times 0.6 \text{ mm} \times 2 \text{ mm}$). Multiple hemorrhages inside the tumor could be identified in the T1-weighted images in the first column of Fig. 8. These hemorrhages with high susceptibilities were successfully reconstructed using xQSM. Substantial streaking artifacts were observed in the MEDI results (orange arrows) and dramatic contrast loss appeared in the U-net reconstruction.

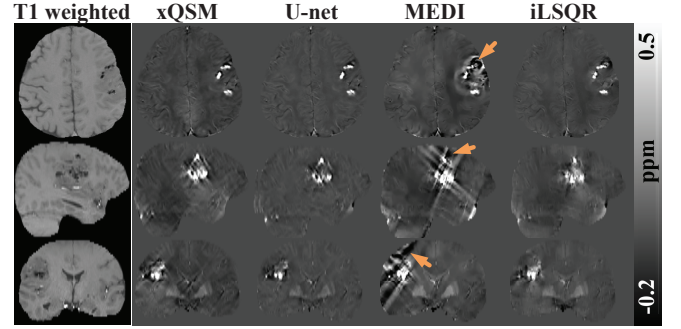


Fig. 8. Demonstration of xQSM, U-net, and traditional methods on an *in vivo* local field map ($0.6 \text{ mm} \times 0.6 \text{ mm} \times 2 \text{ mm}$) from a patient with glioblastoma. Orange arrows point out severe artifacts introduced by MEDI.

IV. DISCUSSION

In this work, we developed a new deep learning framework – xQSM – to perform the ill-posed dipole inversion of QSM reconstruction. The original convolutional layers in a U-net, as used in other deep learning QSM methods [33], [34], [35], [36], were replaced by the modified OctConv [41] layers, which explicitly factorizes the feature maps into high- and low- resolution groups and introduces inter-group operations to allow communication of information between different groups. Such factorization improves the capability of octave networks for multi-scale representation learning [41], which is beneficial for patch-based QSM networks. Our results confirmed that the underestimation present in U-net based methods was successfully recovered by the modified OctConv layers (i.e., xQSM framework).

Some previous deep learning work has been proposed to solve QSM dipole inversion with deep learning, including QSMnet [33], QSMGAN [34], autoQSM [35], and DeepQSM [36]. The first three frameworks require reconstructing QSM first using conventional methods as the training labels, which may deviate from the ground truth. DeepQSM [36] proposed to learn the underpinning physics of dipole inversion with simulated synthetic data. The DeepQSM scheme has two main advantages: i) the training input and the output satisfies the physics relationship between field and susceptibility source, and ii) synthetic data generated randomly can be substantially larger for training, than COSMOS or STAR-QSM data acquired and processed from *in vivo* experiments. However, underestimation in DGM was reported in DeepQSM method. Our xQSM technique enhances the U-net-based DeepQSM results, recovering the significant underestimation in DGM, especially in GP. Our results on human brain data (simulated and *in vivo*) showed that the susceptibility underestimation in GP region in U-net_{synthetic} (nearly 33% underestimation on average), as proposed in DeepQSM [36], was alleviated via using *in vivo* training datasets (about 14% underestimation), or incorporating the proposed modified OctConv (around 21% underestimation), or combining both strategies (less than 3% underestimation).

The improvement from networks based on synthetic data to the networks trained with *in vivo* data was expectable because the networks could learn more brain features, which was

beneficial for reconstructing human brain data in the testing phase. The improvement from U-nets to xQSM networks may originate from the feature factorization design in OctConv (4). Owing to this factorization, one xQSM network indeed comprises two sub-U-nets of the same topology that are connected layer by layer via the F_{HL} and F_{LH} of (4). One of the sub-U-nets operates on high-resolution features as the traditional U-net does (with only half the number of filters each layer), while the other sub-U-net can learn from the low-resolution features. The effective receptive field for the low-resolution sub-U-net was enlarged by a factor of 2, which helps the network to capture more information from distinct locations [41]. In other words, in traditional U-net, each layer only captures the information from the local receptive field defined by the convolutional kernel size ($3 \times 3 \times 3$ in this work). However, in the proposed xQSM, half of the filters in each layer can gain information from a two times larger receptive field, which reduces the channel-wise redundancy and potentially improves the performance of deep CNNs [41]. The enhancement of the proposed network design is also consistent with a previous study [46], suggesting that multiple branches improve the performance of deep networks.

Various metrics including PSNR, SSIM, and ROI measurements of six DGM regions were compared between xQSM, U-net, iLSQR and MEDI methods. The comparison was tested on (i) simulated data from one COSMOS human brain and 2019 QSM Challenge 2.0 dataset and (ii) *in vivo* human brain data from four healthy subjects, one MS patient, and one glioblastoma patient. The results illustrated in simulated and *in vivo* brain datasets suggest that the proposed xQSM_{in vivo} significantly improved the reconstruction of the original U-net based methods. Furthermore, xQSM_{in vivo} achieves comparable image contrast to MEDI without introducing artifacts. Compared with iLSQR, measurements in the digital brain simulations suggested the image contrast is better preserved via xQSM_{in vivo} (about 12% improvement on average). The reconstruction speed of deep learning based methods is another essential and practical advantage compared with traditional MEDI and iLSQR methods. For example, the reconstruction of xQSM is only 4.2 seconds compared to 129 seconds of iLSQR and over 1000 seconds of MEDI on an image of size $224 \times 304 \times 224$.

The proposed xQSM scheme was also evaluated on a modified Shepp-Logan phantom and a mouse brain to show that the proposed deep networks have learned the underpinning dipole inversion process instead of merely memorizing the features of training sets. For the Shepp-Logan phantom, the proposed xQSM networks performed dramatically better than U-net based methods, and the xQSM_{synthetic} achieved the best error metrics of all methods. This experiment suggested that although the networks trained with *in vivo* data gained better reconstruction on the human brain data, they generalized worse than the networks trained with synthetic data of simpler shapes. This is also the first study to demonstrate successful QSM reconstruction of a mouse brain with deep neural networks trained with human brain QSM data. Although the networks were trained with 1 mm isotropic dataset, it could still be used to reconstruct QSM of various spatial resolutions

(e.g., 0.6 mm isotropic, 0.1 isotropic, and $0.6 \text{ mm} \times 0.6 \text{ mm} \times 2 \text{ mm}$).

One limitation of the current work is the robustness against noise. Our results indicated that when the signal-to-noise ratio of local field map decreases, the quality of the QSM reconstruction by xQSM also decreases, which was also observed in other methods. In the future, different levels of simulated noise could be added into the training datasets to make the framework more robust against noise.

V. CONCLUSION

In this study, we proposed a new deep learning framework – xQSM – for fast and robust QSM image reconstruction. Reduced streaking artifacts, and significantly shortened image reconstruction time, were achieved using the xQSM method for replacing conventional methods. By incorporating modified octave convolutions and training the neural network with *in vivo* brain images through the forward modeling, the proposed xQSM method recovered the susceptibility underestimation in the original U-net-based method with up to 33% enhancement, particularly in the iron-rich deep grey matter region.

ACKNOWLEDGMENT

We thank Steffen Bollmann and Markus Barth for sharing their codes for generating the synthetic training dataset in the present work. We also acknowledge the Queensland Brain Institute at the University of Queensland for providing high-performance GPU computing support.

REFERENCES

- [1] Y. Wang and T. Liu, “Quantitative susceptibility mapping (qsm): decoding mri data for a tissue magnetic biomarker,” *Magnetic resonance in medicine*, vol. 73, no. 1, pp. 82–101, 2015.
- [2] C. Liu, H. Wei, N.-J. Gong, M. Cronin, R. Dibb, and K. Decker, “Quantitative susceptibility mapping: contrast mechanisms and clinical applications,” *Tomography*, vol. 1, no. 1, p. 3, 2015.
- [3] A. M. Elkady, D. Cobzas, H. Sun, P. Seres, G. Blevins, and A. H. Wilman, “Five year iron changes in relapsing-remitting multiple sclerosis deep gray matter compared to healthy controls,” *Multiple sclerosis and related disorders*, vol. 33, pp. 107–115, 2019.
- [4] A. M. Elkady, D. Cobzas, H. Sun, G. Blevins, and A. H. Wilman, “Discriminative analysis of regional evolution of iron and myelin/calcium in deep gray matter of multiple sclerosis and healthy subjects,” *Journal of Magnetic Resonance Imaging*, vol. 48, no. 3, pp. 652–668, 2018.
- [5] C. Langkammer, T. Liu, M. Khalil, C. Enzinger, M. Jehna, S. Fuchs, F. Fazekas, Y. Wang, and S. Ropele, “Quantitative susceptibility mapping in multiple sclerosis,” *Radiology*, vol. 267, no. 2, pp. 551–559, 2013.
- [6] J. Acosta-Cabronero, G. B. Williams, A. Cardenas-Blanco, R. J. Arnold, V. Lupson, and P. J. Nestor, “In vivo quantitative susceptibility mapping (qsm) in alzheimer’s disease,” *PLoS one*, vol. 8, no. 11, 2013.
- [7] J. Acosta-Cabronero, A. Cardenas-Blanco, M. J. Betts, M. Butryn, J. P. Valdes-Herrera, I. Galazky, and P. J. Nestor, “The whole-brain pattern of magnetic susceptibility perturbations in parkinsons disease,” *Brain*, vol. 140, no. 1, pp. 118–131, 2017.
- [8] M. Juhás, H. Sun, M. R. Brown, M. B. MacKay, K. F. Mann, W. H. Sommer, A. H. Wilman, S. M. Dursun, and A. J. Greenshaw, “Deep grey matter iron accumulation in alcohol use disorder,” *NeuroImage*, vol. 148, pp. 115–122, 2017.
- [9] S. Chang, J. Zhang, T. Liu, A. J. Tsiouris, J. Shou, T. Nguyen, D. Leifer, Y. Wang, and I. Kovanlikaya, “Quantitative susceptibility mapping of intracerebral hemorrhages at various stages,” *Journal of Magnetic Resonance Imaging*, vol. 44, no. 2, pp. 420–425, 2016.
- [10] H. Sun, A. C. Klahr, M. Kate, L. C. Gioia, D. J. Emery, K. S. Butcher, and A. H. Wilman, “Quantitative susceptibility mapping for following intracranial hemorrhage,” *Radiology*, vol. 288, no. 3, pp. 830–839, 2018.

- [11] H. Sun, J. O. Cleary, R. Glarin, S. C. Kolbe, R. J. Ordidge, B. A. Moffat, and G. B. Pike, "Extracting more for less: multi-echo mp2rage for simultaneous t1-weighted imaging, t1 mapping, mapping, swi, and qsm from a single acquisition," *Magnetic resonance in medicine*, 2019.
- [12] H. S. Abdul-Rahman, M. A. Gdeisat, D. R. Burton, M. J. Lalor, F. Lilley, and C. J. Moore, "Fast and robust three-dimensional best path phase unwrapping algorithm," *Applied optics*, vol. 46, no. 26, pp. 6623–6635, 2007.
- [13] F. Schweser, A. Deistung, B. W. Lehr, and J. R. Reichenbach, "Quantitative imaging of intrinsic magnetic tissue properties using mri signal phase: an approach to in vivo brain iron metabolism?," *Neuroimage*, vol. 54, no. 4, pp. 2789–2807, 2011.
- [14] H. Sun and A. H. Wilman, "Background field removal using spherical mean value filtering and tikhonov regularization," *Magnetic resonance in medicine*, vol. 71, no. 3, pp. 1151–1157, 2014.
- [15] T. Liu, I. Khalidov, L. de Rochefort, P. Spincemaille, J. Liu, A. J. Tsiouris, and Y. Wang, "A novel background field removal method for mri using projection onto dipole fields," *NMR in Biomedicine*, vol. 24, no. 9, pp. 1129–1136, 2011.
- [16] D. Zhou, T. Liu, P. Spincemaille, and Y. Wang, "Background field removal by solving the laplacian boundary value problem," *NMR in Biomedicine*, vol. 27, no. 3, pp. 312–319, 2014.
- [17] T. Liu, P. Spincemaille, L. De Rochefort, B. Kressler, and Y. Wang, "Calculation of susceptibility through multiple orientation sampling (cosmos): a method for conditioning the inverse problem from measured magnetic field map to susceptibility source image in mri," *Magnetic Resonance in Medicine: An Official Journal of the International Society for Magnetic Resonance in Medicine*, vol. 61, no. 1, pp. 196–204, 2009.
- [18] W. Li, C. Liu, T. Q. Duong, P. C. van Zijl, and X. Li, "Susceptibility tensor imaging (sti) of the brain," *NMR in Biomedicine*, vol. 30, no. 4, p. e3540, 2017.
- [19] W. Li, N. Wang, F. Yu, H. Han, W. Cao, R. Romero, B. Tantiwongkosi, T. Q. Duong, and C. Liu, "A method for estimating and removing streaking artifacts in quantitative susceptibility mapping," *Neuroimage*, vol. 108, pp. 111–122, 2015.
- [20] J. Liu, T. Liu, L. de Rochefort, J. Ledoux, I. Khalidov, W. Chen, A. J. Tsiouris, C. Wisnieff, P. Spincemaille, M. R. Prince, *et al.*, "Morphology enabled dipole inversion for quantitative susceptibility mapping using structural consistency between the magnitude image and the susceptibility map," *Neuroimage*, vol. 59, no. 3, pp. 2560–2568, 2012.
- [21] C. Langkammer, K. Bredies, B. A. Poser, M. Barth, G. Reishofer, A. P. Fan, B. Bilgic, F. Fazekas, C. Mainero, and S. Ropele, "Fast quantitative susceptibility mapping using 3d epi and total generalized variation," *Neuroimage*, vol. 111, pp. 622–630, 2015.
- [22] Z. Liu, Y. Kee, D. Zhou, Y. Wang, and P. Spincemaille, "Preconditioned total field inversion (TFI) method for quantitative susceptibility mapping," *Magnetic resonance in medicine*, vol. 78, no. 1, pp. 303–315, 2017.
- [23] H. Sun, Y. Ma, M. E. MacDonald, and G. B. Pike, "Whole head quantitative susceptibility mapping using a least-norm direct dipole inversion method," *NeuroImage*, vol. 179, pp. 166–175, 2018.
- [24] M. T. McCann, K. H. Jin, and M. Unser, "Convolutional neural networks for inverse problems in imaging: A review," *IEEE Signal Processing Magazine*, vol. 34, no. 6, pp. 85–95, 2017.
- [25] D. Shen, G. Wu, and H.-I. Suk, "Deep learning in medical image analysis," *Annual review of biomedical engineering*, vol. 19, pp. 221–248, 2017.
- [26] C. Dong, C. C. Loy, K. He, and X. Tang, "Image super-resolution using deep convolutional networks," *IEEE transactions on pattern analysis and machine intelligence*, vol. 38, no. 2, pp. 295–307, 2015.
- [27] K. Zhang, W. Zuo, Y. Chen, D. Meng, and L. Zhang, "Beyond a gaussian denoiser: Residual learning of deep cnn for image denoising," *IEEE Transactions on Image Processing*, vol. 26, no. 7, pp. 3142–3155, 2017.
- [28] L. Xu, J. S. Ren, C. Liu, and J. Jia, "Deep convolutional neural network for image deconvolution," in *Advances in Neural Information Processing Systems 27* (Z. Ghahramani, M. Welling, C. Cortes, N. D. Lawrence, and K. Q. Weinberger, eds.), pp. 1790–1798, Curran Associates, Inc., 2014.
- [29] Y. Han, L. Sunwoo, and J. C. Ye, "k-space deep learning for accelerated mri," *IEEE transactions on medical imaging*, vol. 39, no. 2, pp. 377–386, 2019.
- [30] B. Zhu, J. Z. Liu, S. F. Cauley, B. R. Rosen, and M. S. Rosen, "Image reconstruction by domain-transform manifold learning," *Nature*, vol. 555, no. 7697, pp. 487–492, 2018.
- [31] S. Ravishanker, J. C. Ye, and J. A. Fessler, "Image reconstruction: From sparsity to data-adaptive methods and machine learning," *Proceedings of the IEEE*, vol. 108, no. 1, pp. 86–109, 2019.
- [32] K. H. Jin, M. T. McCann, E. Froustey, and M. Unser, "Deep convolutional neural network for inverse problems in imaging," *IEEE Transactions on Image Processing*, vol. 26, no. 9, pp. 4509–4522, 2017.
- [33] J. Yoon, E. Gong, I. Chatnuntawech, B. Bilgic, J. Lee, W. Jung, J. Ko, H. Jung, K. Setsompop, G. Zaharchuk, *et al.*, "Quantitative susceptibility mapping using deep neural network: Qsmnet," *Neuroimage*, vol. 179, pp. 199–206, 2018.
- [34] Y. Chen, A. Jakary, S. Avadiappan, C. P. Hess, and J. M. Lupo, "Qsmgan: Improved quantitative susceptibility mapping using 3d generative adversarial networks with increased receptive field," *NeuroImage*, vol. 207, p. 116389, 2020.
- [35] H. Wei, S. Cao, Y. Zhang, X. Guan, F. Yan, K. W. Yeom, and C. Liu, "Learning-based single-step quantitative susceptibility mapping reconstruction without brain extraction," *NeuroImage*, vol. 202, p. 116064, 2019.
- [36] S. Bollmann, K. G. B. Rasmussen, M. Kristensen, R. G. Blendl, L. R. Østergaard, M. Plochanski, K. O'Brien, C. Langkammer, A. Janke, and M. Barth, "Deepqsm-using deep learning to solve the dipole inversion for quantitative susceptibility mapping," *NeuroImage*, vol. 195, pp. 373–383, 2019.
- [37] O. Ronneberger, P. Fischer, and T. Brox, "U-net: Convolutional networks for biomedical image segmentation," in *Medical Image Computing and Computer-Assisted Intervention – MICCAI 2015* (N. Navab, J. Hornegger, W. M. Wells, and A. F. Frangi, eds.), (Cham), pp. 234–241, Springer International Publishing, 2015.
- [38] I. Goodfellow, J. Pouget-Abadie, M. Mirza, B. Xu, D. Warde-Farley, S. Ozair, A. Courville, and Y. Bengio, "Generative adversarial nets," in *Advances in Neural Information Processing Systems 27* (Z. Ghahramani, M. Welling, C. Cortes, N. D. Lawrence, and K. Q. Weinberger, eds.), pp. 2672–2680, Curran Associates, Inc., 2014.
- [39] H. Wei, R. Dibb, Y. Zhou, Y. Sun, J. Xu, N. Wang, and C. Liu, "Streaking artifact reduction for quantitative susceptibility mapping of sources with large dynamic range," *NMR in Biomedicine*, vol. 28, no. 10, pp. 1294–1303, 2015.
- [40] J. Marques and R. Bowtell, "Application of a fourier-based method for rapid calculation of field inhomogeneity due to spatial variation of magnetic susceptibility," *Concepts in Magnetic Resonance Part B: Magnetic Resonance Engineering: An Educational Journal*, vol. 25, no. 1, pp. 65–78, 2005.
- [41] Y. Chen, H. Fan, B. Xu, Z. Yan, Y. Kalantidis, M. Rohrbach, S. Yan, and J. Feng, "Drop an octave: Reducing spatial redundancy in convolutional neural networks with octave convolution," in *Proceedings of the IEEE International Conference on Computer Vision*, (Seoul, Korea), pp. 3435–3444, 2019.
- [42] V. Nair and G. E. Hinton, "Rectified linear units improve restricted boltzmann machines," in *Proceedings of the 27th International Conference on International Conference on Machine Learning, ICML10*, (Madison, WI, USA), p. 807814, Omnipress, 2010.
- [43] J. Kim, J. Kwon Lee, and K. Mu Lee, "Accurate image super-resolution using very deep convolutional networks," in *Proceedings of the IEEE conference on computer vision and pattern recognition*, (Las Vegas, Nevada, USA), pp. 1646–1654, 2016.
- [44] K. He, X. Zhang, S. Ren, and J. Sun, "Deep residual learning for image recognition," in *Proceedings of the IEEE conference on computer vision and pattern recognition*, (Las Vegas, Nevada, USA), pp. 770–778, 2016.
- [45] D. P. Kingma and J. Ba, "Adam: A method for stochastic optimization," in *3rd International Conference on Learning Representations, ICLR 2015, San Diego, CA, USA, May 7-9, 2015, Conference Track Proceedings* (Y. Bengio and Y. LeCun, eds.), 2015.
- [46] S. Xie, R. Girshick, P. Dollár, Z. Tu, and K. He, "Aggregated residual transformations for deep neural networks," in *Proceedings of the IEEE conference on computer vision and pattern recognition*, (Honolulu, Hawaii, USA), pp. 1492–1500, 2017.